Weldable and Electrochemically Stable Composite of Graphene and polyvinylidene fluoride as a Current Collector for Promoting Reversible Lithium Plating/Stripping

Qiang Guo[1,2,3], Shuhui Wang[1], Yimei Li[1], Jin Wang[1], Yong Wu[1], Yanan Yu[1], Shengjie Xia[1], Di Hu[2,4], Binjie Hu[2], Zhenya Ye[1], Xufeng Zhou[1,*], George Zheng Chen[3,*] and Zhaoping Liu[1,*]

[1] Key Laboratory of Graphene Technologies and Applications of Zhejiang Province and Advanced Li-ion Battery Engineering Laboratory of Zhejiang Province, Ningbo Institute of Materials Technology and Engineering, Chinese Academy of Sciences (CAS), Ningbo, 315201, China

[2] Department of Chemical and Environmental Engineering, The University of Nottingham Ningbo China, 315100, PR China

[3] Department of Chemical and Environmental Engineering, Faculty of Engineering, The University of Nottingham, Nottingham, NG7 2RD, United Kingdom

[4] Advanced Energy and Environmental Materials & Technologies Research Group, The University of Nottingham Ningbo China, Ningbo, 315100, PR China

Xufeng Zhou E-mail: zhouxf@nimte.ac.cn

George Zheng Chen E-mail: george.chen@nottingham.ac.uk

Zhaoping Liu E-mail: liuzp@nimte.ac.cn

Abstract

Cu foils are physically heavy and chemically inappropriate for lithium metal rechargeable batteries with lithium-metal-free negatrode (LMFRBs). Physically light carbon-based current collectors (CBCCs) with high conductivity and strong resistance toward corrosion by air or electrolyte can replace Cu foil as a preferable deposition substrate for Li. However, welding problems, lithiation or electrolyte penetration-induced mechanical strength reduction, and lithiophobility-induced fragile SEI largely limit the application of CBCCs. In this work, we prepare lightweight graphene/polyvinylidene fluoride (PVDF) composite sheet via a coating and etching process to address the above issues. Cu tabs are bonded firmly to this CBCC with acceptable resistance, guaranteeing practical application. Tightly stacked graphene nanosheets mitigate lithiation and extra Li consumption (SEI), while PVDF as the binder reinforces the mechanical strength of CBCC by hindering the electrolyte penetration. Therefore, this composite CBCC satisfies the basic requirements i.e., sufficient conductivity and mechanical strength, and viable tab welding, needed for pouch cell application. In addition, as a film-forming polymer with a low Fermi level, PVDF helps form Li-F-rich and highly insulating SEI and suppresses electron transfer to the electrolyte, which induces uniform Li^+ flux and alleviates electrolyte decomposition. The stable interface and robust SEI give rise to uniform and more reversible Li plating/stripping. The assembled LMFRB using this composite CBCC achieves remarkable capacity retention of 80% after ~50 cycles with a high plating capacity of 4 mAh cm^{-2}.

KEYWORDS: graphene, polyvinylidene fluoride, carbon-based current collectors, corrosion, Li metal rechargeable batteries with a lithium-metal-free negatrode.

1 Introduction

With the expanding popularity of electronic devices and electric vehicles, conventional lithium ion (Li^+) batteries are not keeping up with the emerging demand for higher energy density. Lithium (Li) metal, as the ultimate negative electrode (negatrode) for high energy density battery systems, is arousing wide attention owing to its very negative potential (−3.04 V vs. standard hydrogen electrode) and high theoretical specific capacity (3860 mAh g^{-1}) as well as low density (0.53 g cm^{-3}).[1] Meanwhile, lithium metal rechargeable batteries with lithium-metal-free negatrode (LMFRBs) have shown profound advantages due to their higher energy density and s

manufacturing cost than conventional lithium metal rechargeable batteries (LMRBs).[2]

However, implementation of a practical Li negatrode is impeded by the unavoidable deposition of dendritic Li which can penetrate the separator and give rise to internal short circuits. Also, on a Li negatrode continuous formation of inactive Li pieces occurs, which causes low coulombic efficiency (CE) and fast capacity fading during Li plating/stripping.[3, 4] Conceivably, compared with the conventional LMRBs, it is more challenging for LMFRBs to deliver a long cycle life without Li compensation.

Recently, various approaches have been reported to alleviate the formation of Li dendrites in LMFRBs, such as current collector engineering,[4-9] preparation of artificial interface,[10, 11] electrolyte formulations,[12-14] and modifying charge/discharge protocols.[15, 16] Undoubtedly, current collectors as an essential component are worth focusing on in LMFRBs since they can highly impact the reversibility of Li deposition. Not only can the current collector play a role in conducting electrons, but also directly affect the Li deposition behaviour on the substrate in LMFRBs.[2, 17]

Cu foils are a commonly used current collector in Li ion batteries and indeed function well due to their high conductivity and good mechanical property. However, Cu foil is inappropriate to serve as a suitable deposition substrate for Li in LMFRBs as it is prone to be corroded by air or electrolyte, which will destroy the formation of a robust SEI and increase the irreversible capacity. Non-uniform current distribution on bare Cu foil can further exacerbate Li deposition. Equally important, heavy Cu foils can impair the specific energy of LMFRBs. In past years, researchers have employed numerous strategies to modify Cu foil such as plating a tin layer,[5] growing multilayer graphene

via chemical vapour deposition,[18] and coating PAN fibre array via electrospinning.[19] However, these strategies are too complicated to apply in the industry. Meanwhile, the mass loading and thickness of modified current collectors can hardly meet the specific energy requirement at the cell level.[17] More importantly, it is commonly overlooked that galvanic corrosion between the metal-based current collector and electroplated Li in the presence of electrolyte leads to Li dissolution and reduction of cell capacity.[20]

It has been extensively proposed that highly conductive and light-weight carbon-based current collectors (CBCCs) such as graphene paper,[21] carbon cloth,[22] and carbon nanotubes (CNTs) films[23] can replace Cu foil in Li batteries with the advantage of raising specific energy. Furthermore, carbon materials perform better resistance toward corrosion by air or electrolyte,[20, 24] better heat dissipation (high thermal conductivity) capability, and more uniform current distribution than metal-based current collectors.[25]

Nevertheless, the implementation of CBCCs is still hindered due to two inherent issues. The first one is tab welding. Unlike metallic materials that melt at high temperatures, carbon materials are difficult to be melted. Consequently, the conventional welding process does not apply to connecting carbon materials and metal tabs, which poses a big problem for the practical application of CBCCs. The other issue is related to the Li deposition behaviours on carbon substrates. Firstly, due to their lithiophobic property,[26] it is challenging to have stable Li deposition/dissolution on pure carbon substrates. Because the basal plane of graphitic carbon materials has a high energy barrier for Li nucleation, Li deposits tend to form a dendritic morphology, leading to fragile SEI.[26] Secondly, it is found that Li^+ insertion (lithiation) in graphitic

carbon materials will easily give rise to the degradation of their mechanical properties.[27] Also, penetration of electrolytes into the interior of CBCCs often leads to dramatic volume expansion. Thus cracking or even pulverization of CBCCs may occur during cycling, which makes it difficult to sustain a long cycling lifespan.[28] Therefore, it is feasible to introduce polymers that are stable toward electrolytes and can suppress Li^+ insertion in carbon materials to enhance the structural stability of CBCCs. It will be more helpful if the polymers can improve the reversibility of Li plating/stripping in the meantime.

Herein, we propose a simple strategy of using polyvinylidene fluoride (PVDF) as an excellent binder/film-forming additive in the graphene-based free-standing CBCCs. Graphene sheets with high electrical conductivity are tightly stacked, which considerably reduces the electrochemically reactive surface area to decrease the extra SEI formation in comparison with 3D CBCCs assembled by CNTs or carbon fibres. PVDF can not only sufficiently bind the graphene sheets to form the sturdy free-standing film but also hinder the lithiation/electrolyte penetration to the inside of CBCCs to maintain good mechanical properties during cycling. Meanwhile, the Li-F components derived from the partial reduction of PVDF with deposited Li in SEI can decline the lithiophobility-induced fragile SEI and improve the Li reversibility of LMFRBs. Also, this CBCC can suppress electron transfer to the electrolyte, which minimizes the electrolyte decomposition and induces uniform Li^+ flux owing to the low Fermi level of PVDF. It is also worth mentioning that by partially etching the Cu substrate, Cu tabs can be bonded firmly to the CBCCs with acceptable resistance,

guaranteeing its practical application in pouch cells.

Therefore, more reversible Li plating/stripping can be achieved on graphene/PVDF composite current collector compared with bare Cu foil or bare graphene current collector as illustrated in Fig. 1. It is well known that Li deposits on Cu foil with dentritic morphology due to the continuous formation of fragile and unstable SEI. Ultimately, a large amount of whisker-like “dead Li” which blocks electron transportation and Li-ion diffusion will be formed after cycles, leading to the failure of the battery (Fig. 1a). Higher resistance to corrosion by air or electrolyte and a more uniform current distribution guarantee a more stable deposition environment on the graphene current collector. Thus, improved Li deposition/dissolution behaviours can be found. But without the help of PVDF, fragile SEI still leads to a large amount of irreversible Li after cycling, along with fragmentation of the graphene current collector due to volume expansion and lithiation (Fig. 1b). PVDF can maintain good mechanical performance during cycling and induce highly insulating Li-F-rich SEI, which triggers uniform Li^+ flux and achieves dendrite-free deposits (Fig. 1c). Thus, improved reversible Li deposition and high specific energy are realized using this free-standing CBCC at the same time.

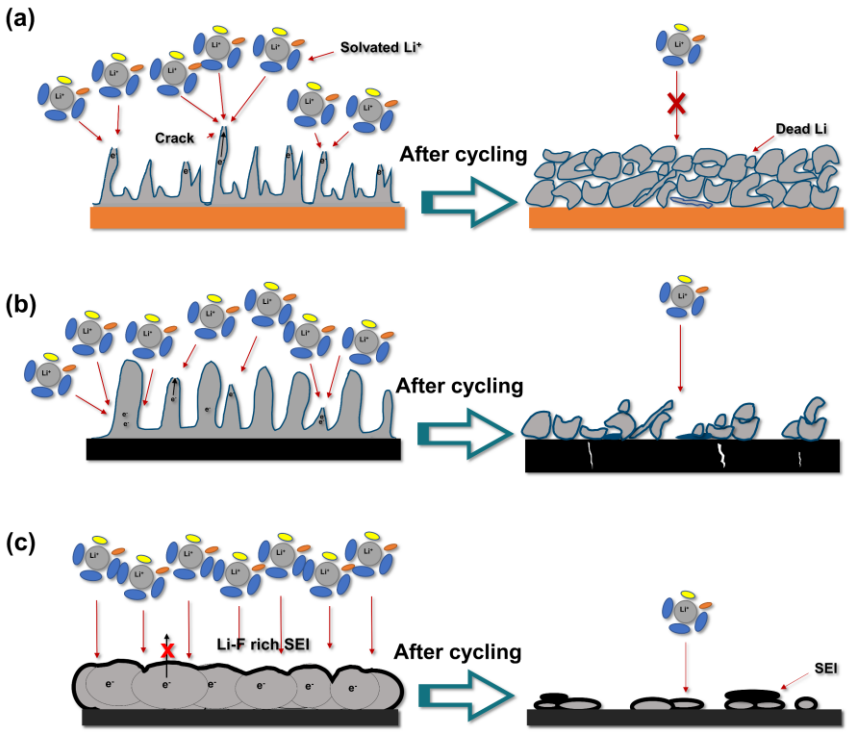

Fig. 1. Schematic diagrams showing the morphology of electrodeposited Li and "dead Li" after cycling on (a) Cu foil, (b) Gra-0/1, and (c) Gra-5/1.

2 Experimental Section

2.1. Electrodes Preparation

Fabrication of the graphene/PVDF composite current collectors (Gra-X/1). Graphene powder (Ningbo Morsh Technology Co., Ltd.) which was stored in an oven at 80 °C for at least 24 h before use, and PVDF (MW:1,000,000) solution (6 wt% in N-methyl-2-pyrrolidone (NMP)) (mass ratio of PVDF: graphene =X:1, X= 1, 5, and 10) were mixed to make the graphene slurry. The slurry with a thickness of 100 μm (mass

ratio of PVDF : graphene = 1:1) or 700 μm (mass ratio of PVDF : graphene =5:1) or 1000 μm (mass ratio of PVDF : graphene = 10:1) was respectively cast on a Cu foil and vacuum-dried at 80 °C for 6 h. The as-obtained electrodes were denoted as Gra-X/1-Cu (X = 1, 5, 10), respectively. The graphene current collector without PVDF (denoted as Gra-0/1-Cu) was also prepared by mixing graphene, carboxymethyl cellulose (CMC), and styrene butadiene rubber (SBR) with a weight ratio of 90 : 5 : 5 to form a homogeneous slurry which was then cast with a thickness of 100 μm on Cu foil and vacuum-dried at 80 °C for 6 h. The as-prepared graphene-based electrodes (GBEs) were soaked in a solution containing 1M $FeCl_3$ and HCl (37 wt%) with the same volume ratio to partially remove the Cu substrate, followed by washing three times with deionized water and vacuum-dried at 80 °C for 6 h. The as-prepared free-standing graphene-based current collectors (GBCCs) were denoted as Gra-X/1 (mass ratio of PVDF : graphene =X:1, X= 0, 1, 5, 10).

Fabrication of the composite current collector of graphene and polyacrylonitrile (PAN) (Gra-5/1-PAN-Cu). Graphene powder which was stored in an oven at 80 °C for at least 24 h before use, and PAN (MW:150,000) solution (6 wt% in N-methyl-2-pyrrolidone (NMP)) (mass ratio of PAN : graphene =5:1) were mixed to make the graphene slurry. The slurry with a thickness of 700 μm was cast on a Cu foil and vacuum-dried at 80 °C for 6 h. The as-obtained electrodes were denoted as Gra-5/1-PAN-Cu.

The as-prepared Gra-X/1-Cu or Gra-X/1 (X = 0, 1, 5, and 10) or Gra-5/1-PAN-Cu were punched into 14 mm discs or cut to 47 mm × 57 mm or 64 mm × 74 mm sheets,

respectively for application as the current collectors in coin-type or pouch cells. Other CBCCs such as carbon cloth (Suzhou Sinero Technology Co., Ltd.), CNTs film (Nanjing Yuanchang New Materials Co., Ltd.), expanded graphite paper (Hefei Aoqi Electronic Technology Co., Ltd.), graphene paper (prepared by vacuum filtration of aqueous graphene slurry), and graphite paper (Ningbo Morsh Technology Co., Ltd.) were also punched into 14 mm discs or cut to 47 mm × 57 mm sheets for comparison.

Fabrication of $LiFePO_4$ (LFP), $LiNi_{0.8}Co_{0.1}Mn_{0.1}O_2$ (NCM 811), and $Li_{1.14}Ni_{0.13}Co_{0.13}Mn_{0.54}O_2$ (LR-NCM 114) positive electrodes. LFP slurry was prepared by mixing LFP powders (Shenzhen BTR New Energy Materials Inc.), Super P, and PVDF in NMP with a mass ratio of 8:1:1 and coated on Al foil with a thickness of 700 μm. The as-obtained LFP electrode was punched into discs with a diameter of 14 mm as the LFP positive electrode. The areal loading of the LFP positive electrode was 12 mg cm^{-2}, corresponding to an areal capacity of ~ 2 mAh cm^{-2}. NCM 811 (Ningbo Ronbay Lithium Battery Material Co., Ltd.) slurry was prepared by mixing Ni-rich oxides, Super P, single-walled carbon nanotubes (SWCNTs), CNTs, and PVDF in NMP with a weight ratio of 97.80 : 0.40 : 0.02 : 0.28 : 1.50, and coated on Al foil. The as-obtained NCM 811 electrodes were punched into discs with a diameter of 14 mm as the NCM 811 positive electrodes. Alternatively, the as-prepared NCM 811 electrode was tailored in 43 mm × 53 mm as the positive electrode in NCM 811-based pouch cells. Single side areal loading of the positive electrode was ~20 mg cm^{-2}, corresponding to an areal capacity of ~4 mAh cm^{-2}. $Li_{1.14}Ni_{0.13}Co_{0.13}Mn_{0.54}O_2$ (LR-NCM 114) (Ningbo Fuli Battery Material Co., Ltd.) slurry was prepared by mixing Li-

rich oxides, Super P, and PVDF in NMP with a weight ratio of 96 : 2 : 2, and coated on Al foil. The as-obtained LR-NCM 114 electrodes were tailored to 62 mm×72 mm as the positive electrodes in LR-NCM-114-based pouch cells. The areal capacity of the LR-NCM 114 positive electrode was ~6 mAh cm^{-2}.

2.2. Electrochemical Measurements

Two-electrode coin half cells (Li vs. Gra-X/1 or Gra-X/1-Cu (X = 0, 1, 5, and 10) or Gra-5/1-PAN-Cu). Standard CR2032 coin-type cells were assembled in an Ar-filled glove box with H_2O and O_2 content below 1 ppm. For the Li||Cu or Li||C coin half cell, a 0.5 mm thick Li disc with a diameter of 16.0 mm was applied as both the counter and reference electrode. The as-obtained 14 mm discs of Gra-X/1 or Gra-X/1-Cu (X = 0, 1, 5, and 10) or Gra-5/1-PAN-Cu were employed as the working electrode. Polypropylene membrane (Celgard 2500) with a thickness of 25 μm was applied as the separator. 1 M lithium hexafluorophosphate ($LiPF_6$) in fluoroethylene carbonate and ethyl methyl carbonate (FEC: EMC=1: 5, v/v) (Zhangjiagang Guotai-Huarong New Chemical Materials Co., Ltd) was employed as the ester-based electrolyte in Li||Cu or Li||C coin half cells. In addition, 1 M lithium bis(trifluoromethanesulphonyl)imide (LiTFSI) in 1,3-dioxolane (DOL)/dimethoxyethane (DME) (v/v = 1:1) with 2.0 wt.% $LiNO_3$ additive was applied as the contrastive ether-based electrolyte in coin half cells. 75 μL electrolyte was added to each cell. All coin cells were shelved for 8 h before testing. The cells were first cycled at 0-3.0 V (versus Li^+/Li) at 0.1 mA cm^{-2} for ten cycles to remove surface contamination in Li||Cu or Li||C coin half cell. The galvanostatic performances were conducted at 25 °C using the Land CT 2100A system (Jinnuo

Wuhan Corp, China). Li was plated galvanostatically with capacities of 1 or 3 mAh cm^{-2} and then stripped galvanostatically with a cut-off potential of 0.5 V vs. Li/Li^+ at different current densities. Cyclic voltammetry (CV) and electrochemical impedance spectroscopy (EIS) were tested by an electrochemical workstation (Solartron 1470E) using CR2032-type coin cells. The voltage range of CV was chosen from 2 V to −0.25 V with a scan rate of 0.1 mV s^{-1}. The frequency range was set between 1 MHz and 0.01 Hz.

Two-electrode coin full cells (LFP or NCM 811 vs. Cu or Gra-X/1 or Gra-X/1-Cu (X = 0, 1, 5, and 10)). In Cu or Gra-X/1 or Gra-X/1-Cu (X = 0, 1, 5, and 10) ||LFP or NCM 811 coin full cells, the as-prepared 14 mm discs of Cu or Gra-X/1 or Gra-X/1-Cu (X = 0, 1, 5 and 10) and LFP or NCM 811 were employed as the current collectors and positive electrodes, respectively. Polypropylene membrane (Celgard 2500) was used as the separator (25 μm). The electrolyte used herein was 1 M $LiPF_6$ in a mixed solution of FEC and EMC (volume ratio of 1:5). Electrolyte injection was fixed at 75 μL in each coin cell. All coin cells were shelved for 8 h before testing. The cycling performances of the LFP-based full cells were galvanostatically charged up to 4 V at 0.5 C and then galvanostatically discharged to 2.0 V at 1C. The NCM 811-based full cells were galvanostatically charged up to 4.3 V and then galvanostatically discharged to 2.6 V at various rates from 0.1 C to 2 C. Cycling performances of the cells were tested by charging at 0.1 C and discharging at 0.2 C within the voltage range from 2.6 to 4.3 V.

Pouch cells (NCM 811 or LR-NCM 114 vs. Gra-5/1 or Gra-5/1-Cu or Gra-5/1-

PAN-Cu). Gra-5/1, Gra-5/1-Cu, or Gra-5/1-PAN-Cu with a size of 47 mm × 57 mm or 64 mm × 74 mm were employed as the current collectors. As-prepared NCM 811 electrodes with 43 mm × 53 mm were applied as the positive electrode. Polypropylene membrane (Celgard 2500) was used as the separator (25 μm). 1 M $LiPF_6$ in FEC/EMC=1:5 by volume was used as the electrolyte (6 g Ah^{-1}). Alternatively, lithium bis(fluorosulfonyl)imide (LiFSI), DMC, and 1,1,2,2-tetrafluoroethyl-2,2,3,3-tetrafluoropropylether (TTE) with a molar ratio of 3:4:1 with 1wt% lithium difluoro(oxalato)borate (LiDFOB) were used as a modified electrolyte. After injecting the electrolyte, full cells were at least stored for two days to achieve full infiltration of electrolytes into pores of separators and positive electrodes. The NCM 811-based pouch cells were galvanostatically charged up to 4.3 V and then galvanostatically discharged to 2.6 V at 0.1 or 0.2 C. The LR-NCM 114-based pouch cells with a positive electrode size of 62 mm × 72 mm were galvanostatically charged up to 4.6 V at 0.1C and then galvanostatically discharged to 2.6 V at 0.1 C. Pouch cells were subjected to 100 kPa pressure during charging/discharging.

2.3. Sample Characterization

The microscopic morphology of samples was characterized by a Hitachi S-4800 field emission scanning electron microscope (SEM). X-ray diffraction (XRD) patterns of samples were recorded using an AXS D8 Advance diffractometer (Cu Kα radiation; receiving slit, 0.2 mm; scintillation counter; 40 mA, 40 kV) from Bruker Inc. Transmission electron microscope (TEM) (FEI Tecnai F20) operating at 200 kV was employed to measure the layer number and lateral size of graphene sheets. The

measurements of X-ray photoelectron spectroscopy (XPS) (Axis Ultra DLD) were conducted using Al Kα monochromatic beam (1,486.6 eV) and C 1s peak (284.8 eV) to calibrate. The Renishaw in Via Reflex micro-Raman spectrometer equipped with an exciting laser of 532 nm was employed to characterize the chemical structure of samples. The focused ion beam (FIB) (Helios-G4-CX) was conducted to investigate the intrinsic cross-section view of samples. The atomic force microscope (AFM, Dimension ICON) was used to reveal the physical property of electrodes. The samples' mechanical property was recorded using a 1 kN materials testing machine (Zwick/Roell Z1.0). Surface tension/dynamic contact angle (DCAT21) was employed to show electrolyte wettability toward the samples. Thermogravimetric analysis (TGA) was employed using a thermogravimetric analyzer (TGA209F1) by sealing the samples in a stainless steel crucible in an air atmosphere. The heating rate was 10℃ min^{-1}.

3 Results and Discussion

3.1. Physical Characteristics of Graphene-based Current Collectors

Highly conductive graphene nanosheets prepared by an intercalation and exfoliation method without an oxidation process were used as the raw material to prepare the CBCC. The graphitic structures of graphene materials were characterized by Raman spectroscopy and X-ray diffraction (Fig. S1a-b). Two sharp peaks at 1321 and 1584 cm^{-1} in Fig. S1a are indexed as the D and G bands, respectively. A low-intensity ratio of 0.32 between the two bands (I_D/I_G) indicates the well-ordered graphitic structure,

confirming the high electric conductivity of graphene materials. The XRD result (Fig. S1b) verifies the multilayer structure of the graphene materials as reflected by the characteristic (002) diffraction peak of graphite centred at 26.2° (d= 0.34 nm). The layer number of the graphene sheets was characterized by TEM (Fig. S1c, d) and the results show that graphene sheets are consisted of 7-8 layers with a mean thickness of ~ 3 nm. Meanwhile, TEM image (Figure S1e) with lower magnification shows that a typical graphene sheet has a lateral size of ~2.5 × 2.5 μm.

The graphene powders were mixed with PVDF in NMP solvent with a certain ratio to form a homogeneous slurry. Then the mixture was cast on a Cu foil to form a coating layer after drying. Finally, the free-standing GBCC was prepared by etching the Cu foil using $FeCl_3$ solution, as illustrated in Fig. 2a. Wrinkled graphene sheets are observed on the surface of Gra-5/1 (Fig. 2b), possibly owing to the introduction of PVDF or the use of NMP solvent in the slurry compared to Gra-0/1 in Fig. S2a (using water as the solvent). Magnified SEM image (Fig. 2b) shows that PVDF is attached tightly to the surface of graphene, which guarantees that Li^+ or Li metal can react with PVDF during deposition and mitigate the lithiophobic property of carbon materials. The cross-section view of Gra-5/1 in Fig. 2c shows that the thickness of the as-prepared Gra-5/1 is ~9 μm. The graphene-only coating layer with the same thickness of ~9 μm (see Fig. S2b) was fabricated to make a comparison. Notably, the thickness of graphene-based composite electrodes can be easily controlled on a small scale (<10 μm) by adjusting the coating thickness, which is beneficial to further improve specific energy without sacrificing cost. On the contrary, the thickness and cost of conventional Cu foil are typically

inversely proportional, especially on a small thickness scale (<6 μm).[29] Fig. 2b also manifests the homogeneous mixing of graphene sheets and PVDF. In addition, there are very few pores in the magnified FIB cross-section view of Gra-5/1 in Fig. S3, approving that the obtained Gra-5/1 is non-porous, and can prevent Li^+ inserting/depositing into the interior of the CBCC. The small surface area of Gra-5/1 can also suppress large irreversible Li consumption due to SEI formation. As shown in Fig. 2d, Gra-5/1 (~2.5 mg cm^{-2}, Table S1) is almost 3.5 times lighter than the conventional Cu foil of the same size (47 mm × 57 mm, ~10 μm), which is helpful to increase the specific energy of the battery.

XPS analysis and energy-dispersive spectroscopy (EDS) mapping were carried out to investigate further the chemical composition and electronic states on the surface of Gra-5/1 (Fig. S4-5). One peak at 688.5 eV in the F1s spectrum of Gra-5/1 (Fig. S4a), which is ascribed to the C-F bond, proves the existence of PVDF. The uniform distribution of F and C elements over the entire coating layer is found via EDS mapping, as demonstrated in Fig. S4b-e and Fig. S5a-c, which also agrees with the XPS results. It has been verified that F atoms can interact with Li^+ to form robust SEI components such as Li-F during the electrochemical deposition.[1]

Mechanical properties of Gra-5/1 were also investigated to evaluate its adaptability to the manufacturing procedures of practical cells (Fig. 2e). The excellent flexibility of Gra-5/1 is demonstrated by a bending process with 180 degrees. Though the tensile stress of the CBCCs is lower than metallic Cu foil, the mechanical strength of the as-prepared Gra-5/1 (0.8% at a tensile stress of 15.5 MPa) is sufficient to withstand the

changes of the mechanical stress in the battery during charging/discharging, as well as the production process, which is confirmed by no obvious reduction of tensile strength after cycling over Gra-5/1 (1.6% at a tensile stress of 17.0 MPa). Interestingly, in comparison with the graphene paper (1.2% at a tensile stress of 12.3 MPa) which is physically compressed at high temperatures (Fig. 2e), the free-standing Gra-5/1 shows better tensile strength, which is ascribed to the PVDF molecules that bond graphene sheets. More mechanical characterization, such as DMT modulus, is collected through AFM characterization over bare Cu, Gra-0/1, and Gra-5/1 (Fig. S6a-c) to characterize surface stiffness distribution. Gra-0/1 has the highest micro stiffness (Young's modulus of 112.1 GPa), confirming the excellent mechanical properties of graphene materials[30]. Interestingly, the incorporation of PVDF decreases Young's modulus of Gra-5/1 to 96.7 GPa (Fig. S6b-c) owing to the soft nature of PVDF while keeping good flexibility. The thermal stability of GBCCs is evaluated by TGA (Fig. S7). Gra-5/1 can withstand temperatures up to 400 ºC in an air atmosphere, which is far beyond the normal operating temperatures (<60 ºC) of batteries.

The resistance of CBCCs is an important parameter affecting the energy conversion efficiency and thermal management of the battery. Fig. S8 shows that the resistance of different GBEs is strongly dependent on the mass ratio of PVDF. Specifically, Gra-0/1 with no PVDF exhibits excellent electrical conductivity (resistance of ~2 Ω). As the proportion of PVDF increases, the electrode resistance increases slowly to ~24 Ω (Gra-5/1). When the PVDF/graphene mass ratio reaches 10 (Gra-10/1), the resistance increases sharply to about 138 Ω. Predictably, Gra-10/1 may not be suitable as the

current collector, as it may increase the internal resistance of the battery substantially.

The stable connection between carbon and metallic materials with low resistance is a prerequisite to applying CBCCs in practical pouch cells. Inspired by our previous coating operations on Cu foils,[31] we found that there is strong adhesion and acceptable contact resistance between conductive carbon coatings containing PVDF and Cu foil. Therefore, we decide to leave a small piece of metallic Cu on one end of the GBCC via the coating and etching process to enable tab welding of the CBCCs. The contact resistance between Gra-5/1 and Cu (Fig. 2f) is almost equivalent to the contact resistance between Gra-5/1 and welded metallic tab (Fig. 2g), verifying the reliability of Cu welding in practical pouch cells. Fig. 2f shows that the contact resistance (~0.5 Ω, calculation process see Fig. S9) falls to an acceptable level for pouch cell applications and illustrates the convenience in the fabrication of multi-layer pouch cells.

Overall, this free-standing CBCC is qualified to undertake the basic function of the current collector and show certain processability and practical application potentials in pouch cells.

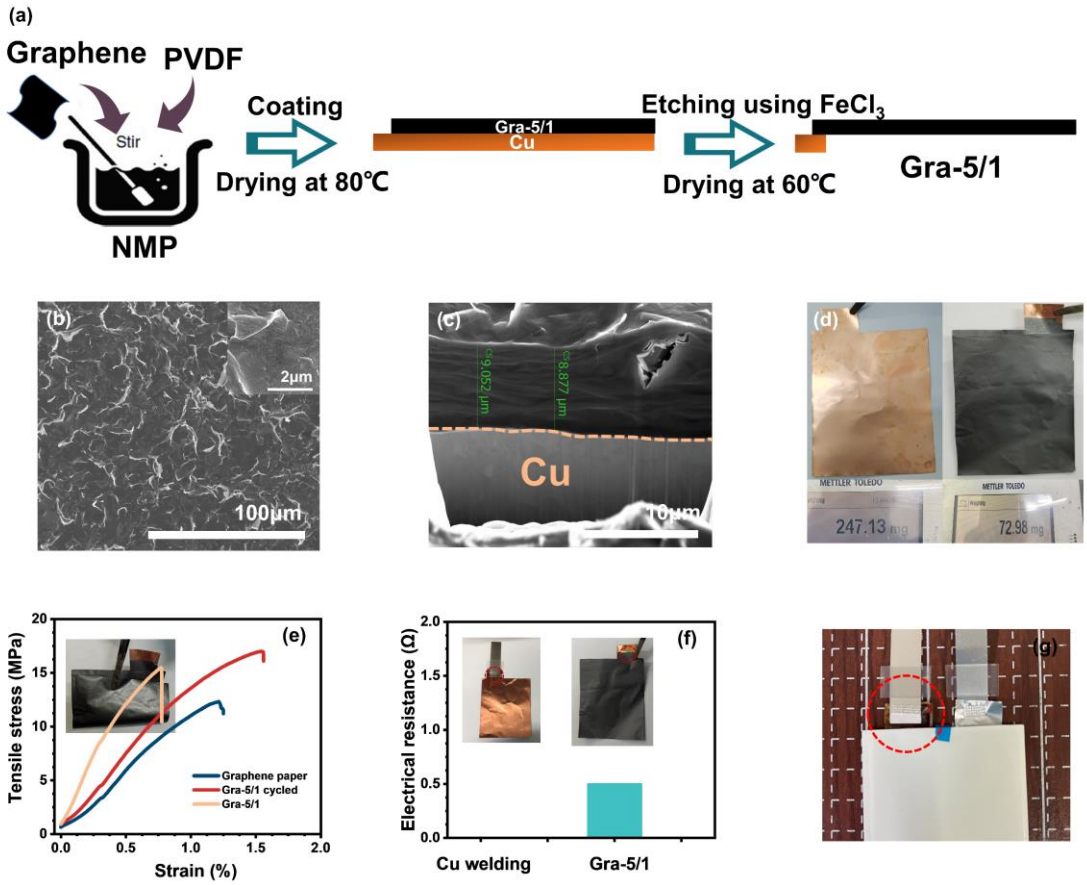

Fig. 2. (a) Schematic illustration of the preparation process of free-standing Gra-5/1. (b) Top-view and (c) cross-section view SEM images of Gra-5/1. The inset of (b) is a high-magnification SEM image. (d) Optical photographs showing the appearance and weight of bare Cu and Gra-5/1. (e) Specific tensile strength of fresh Gra-5/1, cycled Gra-5/1 and graphene paper. (f) Contact resistance between Cu or Gra-5/1 and metallic tabs. The inset optical photographs of (f) show the appearance of different samples. (g) Optical photograph showing the tabs welded on Gra-5/1 in a practical pouch cell.

3.2. The Adaptability of Graphene-based Current Collectors to Cell Operating Conditions

To further estimate the feasibility of the as-fabricated Gra-5/1 as the current collector in practical cells, its adaptability including wettability and stability in the electrolyte or toward Li intercalation was clarified respectively. The contact angle of the electrolyte

toward Gra-5/1 was measured (Fig. S10) to understand further the interaction between the electrolyte and the graphene/PVDF composite current collector. Results show that Gra-5/1 demonstrates considerably better wettability (contact angle of 4°) toward carbonate ester electrolyte compared with Cu foil (contact angle of 23.5°). It was reported that the electrolyte wettability has a close relationship with the uptake amount of liquid electrolyte and then influences the distribution of Li^+ flux over the surface of the entire current collector during cycling.[32] Therefore, such a superior electrolyte wettability is beneficial for uniform Li^+ flux and mitigating uneven Li deposition.

Swelling behaviour is another important parameter that reflects the stability of CBCCs in electrolyte, as electrolyte penetration may cause the volume expansion of CBCCs. Thus, to further evaluate the stability of Gra-5/1 in the electrolyte, the swelling behaviour of Gra-5/1 was measured by soaking it in the electrolyte solution for 15h. Fig. 3a-b illustrates there is no apparent swelling in Gra-5/1, implying PVDF can keep Gra-5/1 stable in the electrolyte by preventing the electrolyte from entering the interior of the current collector. The swelling behaviours of other CBCCs such as graphene paper and CNTs film were also tested to make a comparison with Gra-5/1. Inversely, there is apparent swelling as illustrated in Fig. 3c-d and Fig. S11. It is found that the volume of graphene paper expands by ~30%, and the volume of CNTs film increases by 50%, verifying the fact that PVDF can shield the invasion of electrolytes into the interior of carbon frameworks. Nitrogen adsorption and desorption measurement shows that Gra-5/1 has an extremely low specific surface area and porosity (Fig. 3e), further confirming that electrolytes are not allowed to facilely permeate through this composite

CBCC.

Lithiation/intercalation behavior is rather common in graphite-type materials, but it will give rise to damage to the mechanical strength of CBCCs.[27] Thus, the lithiation behaviour of Gra-5/1 and other free-standing CBCCs was investigated (Fig. 3f and Fig. S12). Interestingly, Gra-5/1 and graphene paper show similar metal-deposition-like behaviour without apparent lithiation potential (Fig. 3f), proving that there is nearly no Li^+ intercalation behaviour. It is probably because horizontally stacked graphene nanosheets can kinetically hinder Li^+ intercalation. This is a good signal for CBCCs to maintain their mechanical strength. However, commercial carbon cloth and CNTs film have apparent lithiation behavior (Fig. S12), implying that their mechanical strength can be largely affected during cycling.

To explore the stability of Gra-5/1 after cycling, we assembled Li||C coin half cells using commercial carbon cloth, CNTs film, graphene paper, and Gra-5/1 respectively as CBCCs to make a comparison. Graphene paper (Fig. 3g), carbon cloth (Fig. S13a), and CNTs film (Fig. S13b) fragmented after cycling. Breakage of carbon cloth and CNTs film can be ascribed to the fact that lithiated CBCCs are too stiff to endure the volume change of Li deposit, which deteriorates their mechanical strength. The reduction of toughness in graphene paper is probably due to the volume expansion caused by electrolyte infiltration. In contrast, Gra-5/1 remained intact after cycling, strongly confirming that non-intercalation of Li^+ and PVDF-induced electrolyte shield/structural reinforcement can help to maintain the mechanical strength of CBCCs continuously (Fig. 3h). Furthermore, the stability of CBCCs toward metallic Li was

investigated by placing Li foils on the top of CBCCs, as shown in Fig. 3i-j and Fig. S13c-d. Again, only Gra-5/1 can maintain its structural integrity after 30 cycles with 3.5 mAh·cm^{-2} of Li plating/stripping at 0.5 mA cm^{-2} due to the PVDF-induced sturdy structure and minimum Li^+ intercalation.[31] Afterward, the flexibility of cycled Gra-5/1 was verified by a simple bending test as shown in Fig. S14. Similar to the original Gra-5/1 (Fig. 2e), the cycled Gra-5/1 still maintains excellent flexibility after 100 cycles in a pouch cell, which elucidates that this free-standing graphene-based composite current collector is strong enough to endure long-term Li deposition/dissolution.

The Li||Cu and Li||C coin half cells were assembled, respectively to further investigate the possible galvanic corrosion between the current collector and electroplated Li in the presence of electrolyte, as it can induce irreversible Li loss and capacity reduction of the cell.[20] The capacity of the discharged cells with electroplated Li on the current collectors before and after standing for 100 hours was measured (Fig. S15). Though the capacity of both cells declines after standing due to electroplated Li involved side reactions, the capacity decay of the Gra-5/1-based cell is reduced by ~30% compared with that of the Cu-based cell, suggesting that the galvanic corrosion reaction taking place between Li and Cu current collector can be eliminated in the case of graphene/PVDF composite current collector. The above results indicate that Gra-5/1 is inert to both electrolyte and Li metal (Fig. 3k), which is crucial to practical applications.

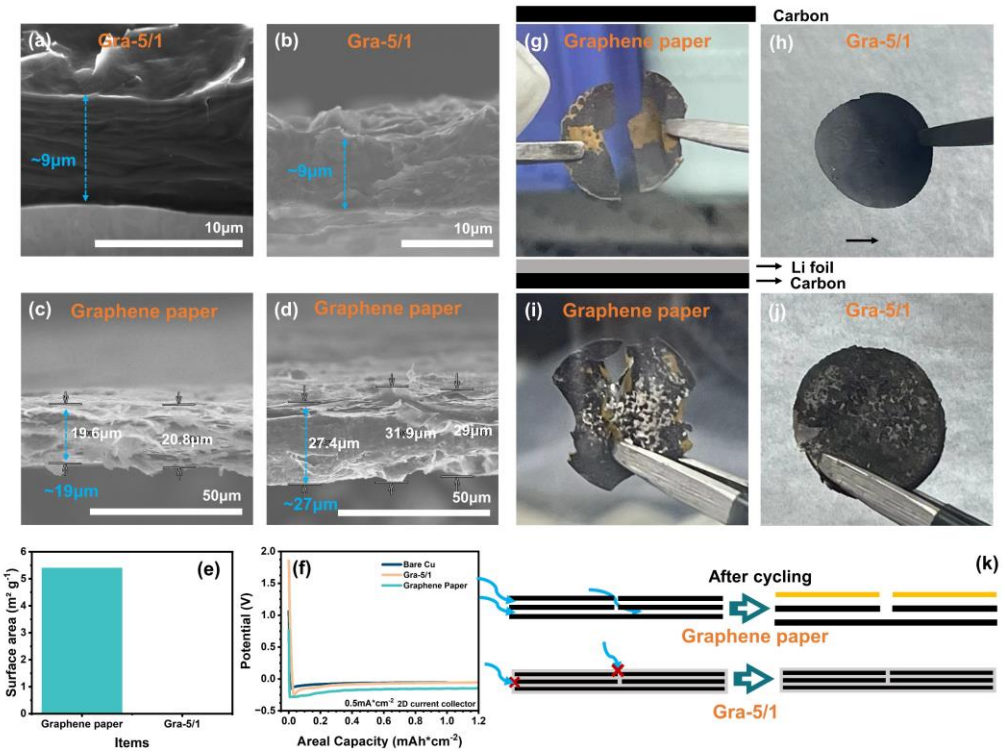

Fig. 3. Electrochemical stability of Gra-5/1 and graphene paper. Cross-section view SEM images of (a, b) Gra-5/1 and (c, d) graphene paper before and after soaking in the electrolyte solution for 15h. (e) Comparison of surface areas of Gra-5/1 and graphene paper. (f) Voltage profiles of Li plating on bare Cu foil, Gra-5/1, and graphene paper with 1.0 mAh cm^{-2} at 0.5 mA cm^{-2}. Optical photograph of graphene paper, and Gra-5/1 after (g, h) 20 cycles of direct Li deposition/dissolution and (i, j) 30 cycles with Li foil covering on the upper surface at 0.5 mA cm^{-2} with 3.5 mAh cm^{-2}. (k) Schematic illustration of the electrode expansion caused by electrolyte infiltration in Gra-5/1 and graphene paper.

3.3. SEI and Li Deposit Characterization

The property and composition of SEI have a strong effect on Li plating/stripping behaviours. Electronic insulation is one of the most important properties of SEI that can prevent electrolyte reduction. Accordingly, the electron insulating property of the SEI relies on the thickness (d) of SEI and Fermi level (E_f) of the electrode surface, as shown

in Eq. (1):[33]

$$T = \frac{16\mathrm{E}_f \Delta E_t}{(\mathrm{E}_f + \Delta E_t)^2} e^{-\frac{4\pi d}{h}\sqrt{2m\Delta E_t}} \quad (1)$$

Where T is the electron tunneling probability for complete electron insulation (namely, $T = e^{-40}$)[33], ΔE_t represents the electron tunneling barrier, m is the mass of an electron, and h is Planck's constant. Thus, the calculation of E_f was conducted to investigate the SEI stability of GBEs, especially toward electrolytes upon cycling (Fig. S16 and Fig. 4a). Fig. S16 displays that Li has the highest theoretical E_f of −2.65 eV[34] among graphene (−4.28 eV), PVDF (−5.90 eV) and Cu[35], which is also higher than the lowest unoccupied molecular orbital (LUMO) of the electrolyte. Thus, the electrolyte is easily reduced by Li via transferring electrons to the LUMO of the electrolyte (Fig. 4b). Real comparative E_f of Cu and GBCCs are obtained in Fig. 4a via testing their comparative work function by AFM. Notably, Gra-5/1 has the lowest E_f, reflecting that Gra-5/1 has the highest antioxidant capability and the lowest electron transfer ability to electrolyte,[36] which provides a relatively stable electrode interface in the beginning. Based on tunneling theory in quantum mechanics, the disparity in the SEI thickness is clarified further. Eq. (1) can be simplified as $T \sim e^{-d\sqrt{\Delta E_t}}$ through the Wentzel–Kramers–Brillouin approximation in quantum tunneling theory.[7, 33] Since ΔE_t increases with decreasing E_f, lower E_f means that electro-insulation can be achieved with a smaller thickness of SEI. In other words, the electrode with lower E_f is more likely to suppress the electron tunneling behaviour of SEI. Therefore, Gra-5/1 may perform the best interfacial compatibility toward electrolytes because it can effectively suppress electron transfer to the LUMO of the electrolyte and avoid the formation of

polymorphous Li with a large surface area (Fig. 4c).

XPS was further conducted to verify the SEI component on Cu foil and GBCCs (Li@Cu, Li@Gra-0/1-Cu, and Li@Gra-5/1-Cu) with a plating areal capacity of 1 mAh cm^{-2} (Fig. 4 d-i). In F 1s spectra (Fig. 4 d-f), Li-F and C-F signals are observed in all electrodes, resulting from the decomposition of FEC or $LiPF_6$.[11] Li-F is well-known as an excellent SEI component owing to its high interfacial energy toward Li and high mechanical strength, which helps suppress Li dendrites. Thus, Li-F-rich SEI is more efficient for uniform Li deposition. According to the literature,[37, 38] the Li-F components can be obtained by the *in-situ* reaction between Li and fluoropolymer (e.g., polytetrafluoroethylene or PVDF). Thus, the highest content of the Li-F (95.7%) in the Li@Gra-5/1-Cu implies that PVDF as a film-forming polymer is involved in the electrochemical deposition and the formation of robust SEI. Li-F is also widely suggested to prevent electron tunneling due to its low solubility and wide band gap (8.9 eV), which further verifies that SEI on Gra-5/1 can suppress electron transfer to the electrolyte. Moreover, In C 1s spectra (Fig. 4 g-i), Li@Gra-5/1-Cu has the lowest intensity of C-C/C-H which mainly comes from the decomposition of electrolyte, confirming that electrolyte reduction can be suppressed by highly insulating SEI. In contrast, the lowest content of the Li-F (73.7%) and the highest content of the C-C/C-H for Li@Cu indicate comparatively unstable SEI and obvious electrolyte reduction. Furthermore, SEI in Li@Gra-5/1-Cu has the smallest interfacial impedance (Fig. S17), showing that electron-retarding property of Gra-5/1 plays a critical role in the evolution of this robust SEI.

The Li nucleation form has an important influence on the subsequent growth mode and surface area exposed to the electrolyte, which was investigated by chronoamperometry test.[39] Fig. S18a demonstrates that the GBCC follows the typical progressive nucleation mode. While Cu foil obeys instantaneous nucleation mode.[40] This difference indicates that new Li nuclei intend to be continuously formed on already existing Li in graphene materials, leading to decreased surface area exposed to the electrolyte. To corroborate the influence of nucleation mode on subsequent Li deposition, the evolution of Li deposition was carried out. Fig. S18b-d exhibits morphology evolution during Li plating with capacities from 0.2 to 1 mAh cm^{-2} on Cu foil, Gra-0/1-Cu, and Gra-5/1-Cu. Due to the non-uniform nucleation of Li, many slender dendrite-like Li are easy to find (0.2 mAh cm^{-2}) on bare Cu (Fig. S18b). Cu has a low work function (high E_f), which makes it easy to trigger electron transfer to the electrolytes.[36] This will not only decrease the insulating property of SEI but also attract a large amount of Li ions. Thus, local whisker protrusion and mossy-type (whisker and dendrite) Li deposits can be found at 0.6 mAh cm^{-2} and 1 mAh cm^{-2}, respectively. Fig. S18c reveals that larger Li particles are observed on Gra-0/1-Cu compared to Cu, which agrees with the Li nucleation mode on graphene. However, with discharging capacity increasing to 0.6 mAh cm^{-2} or 1 mAh cm^{-2}, mossy-type (whisker and dendrite) Li networks still form due to the lack of highly insulated SEI (Li-F-rich SEI). Similar to Gra-0/1-Cu, Fig. S18d reveals that Li can horizontally grow with a small particle size of ~1 μm on Gra-5/1-Cu (0.2 mAh cm^{-2}). When the plating capacity further increases, Li particles gradually become crowded and then splice into a dense and dendrite-free

plane. Besides larger Li nuclei (progressive nucleation mode), Li-F-rich SEI with stronger electron insulation nature also makes Li grow thicker and into a whole on Gra-5/1-Cu (Fig. S18e).

Ex-situ FIB-SEM characterization was further carried out to precisely investigate the morphology of the deposited Li on Cu and GBCCs (Fig. 4j-l). Fig. 4j presents that the porous and dendritic Li is generated on Cu. Besides, remarkably thick SEI covering on porous Li is attributed to the electrolyte decomposition. Thus, SEI with a higher electron tunneling probability not only results in the formation of Li tips but also the generation of by-products (SEI), resulting in poor cycling stability and capacity attenuation in Cu-based LMFRBs.[1] Related EDS mapping result (Fig. S19a) illustrates that F and C are subordinate, while O and Cu account for the two most significant elements in Li@Cu. The high content of Cu strongly supports our previous claim that Cu can be easily electrochemically corroded during plating, while the strong signal of O implies that Li dendrites accelerate the electrolyte decomposition and increase irreversible Li capacity. Compared to the Li@Cu, denser Li deposits can be found due to the larger Li nuclei. However, large voids and thick SEI still can be found on the Li@Gra-0/1-Cu (Fig. 4k). Lower content of O further verifies improved Li deposit morphology (Fig. S19b). In addition, nearly no Cu element can be found in Li@Gra-0/1-Cu, indicating that graphene can effectively prevent Cu from electrochemical corrosion. In striking contrast, the cross-section view of Li plating (Fig. 4l) shows that Li particles tend to splice into a dense and dendrite-free form on Gra-5/1-Cu, which can reduce the contact area between electrolyte and Li (low O content in Fig. S19c). Such

dense Li deposition confirms that highly insulating SEI can decrease the formation of polymorphous Li with a large surface area.

In brief, Cu is unsuitable for Li deposition because of its higher Fermi energy level, lower anti-corrosion property towards air/electrolyte, and difficulty in stabilizing Li deposition without film-forming polymer. Graphene can improve Li deposit morphology, but fragile SEI is incapable of continuously stabilizing Li deposition. Gra-5/1 with good anti-corrosive properties facilitates the formation of a robust and electron-retarding SEI with the assistance of PVDF, which impedes extra electrolyte decomposition and Li inventory consumption, resulting in uniform Li deposition.

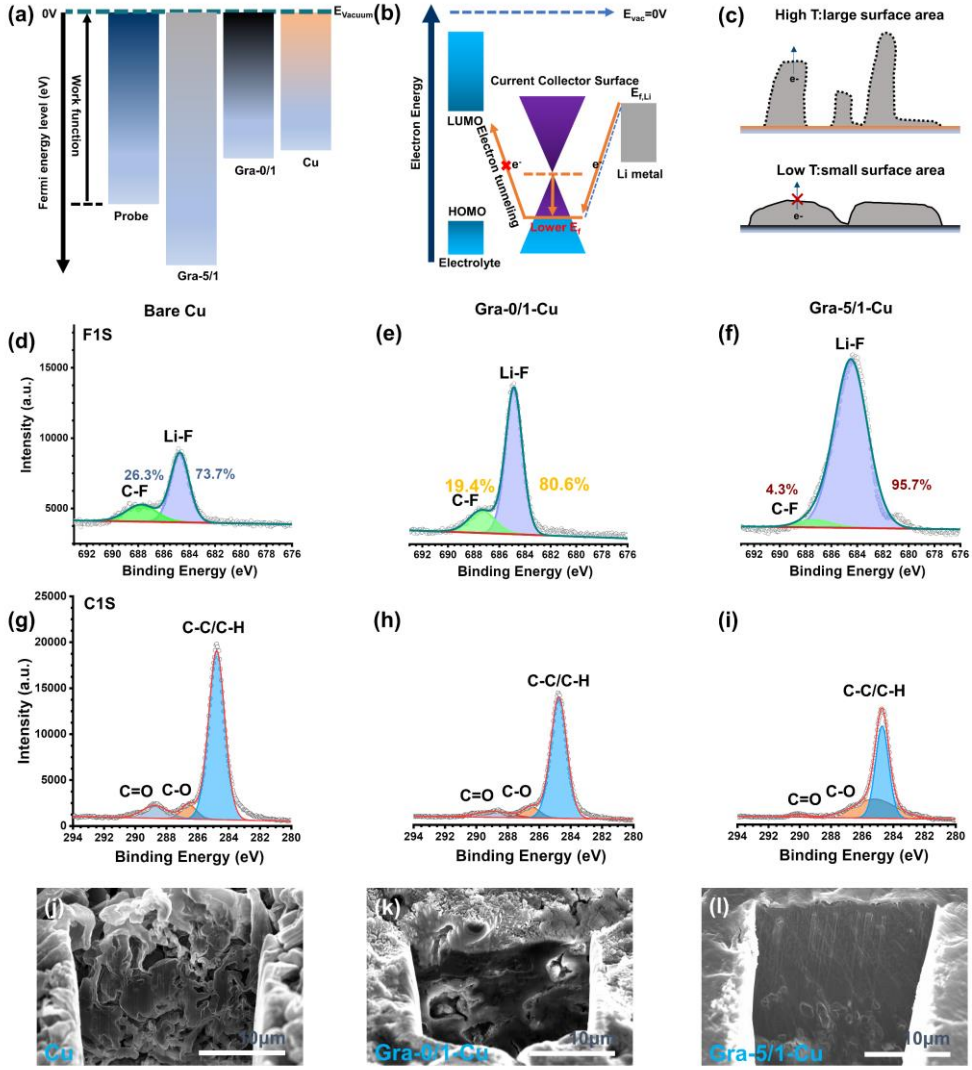

Fig. 4. SEI and Li deposition characterization. (a) Fermi energy level of Gra-5/1, Gra-0/1, and Cu obtained from AFM. (b) Mechanism of lower Fermi level in suppressing electron transfer to the electrolyte on the Gra-5/1. (c) Different Li deposition morphology owing to low and high electron tunneling probability of SEI. XPS spectra of the F 1s and C1s of (d, g) bare Cu, (e, h) Gra-0/1-Cu and (f, i) Gra-5/1-Cu after plating 1 mAh cm^{-2} of Li at 0.5 mA cm^{-2}. Cross-section view FIB-SEM images of (j) bare Cu, (k) Gra-0/1-Cu, and (l) Gra-0/1-Cu with a plating areal capacity of 3 mAh cm^{-2}. The current density is 0.5 mA cm^{-2}.

3.4. Electrochemical Performances of Graphene-based Current Collectors in Half and Full Cells

CE and long-term electrochemical stability of half cells containing different working electrodes (Cu foil and GBEs) coupled with Li foil as the counter electrode was tested. Cu is not etched in the GBEs to eliminate the influence of internal stress in the coin cells. Among all electrodes, Cu foil shows the most severe CE decay, dropping rapidly from an average of ~94% for ~30 cycles to around 90% for only 10 cycles before experiencing a significant decline when the current density is raised from 1 mA cm^{-2} to 2 mA cm^{-2} at 1 mAh cm^{-2} (Fig. 5a and Fig. S20a). This result may be ascribed to the dramatic accumulation of "dead Li". Gra-0/1-Cu keeps comparatively stable CE with an average of ~94.5% within 80 cycles at 1 mA cm^{-2} with 1 mAh cm^{-2} (Fig. 5a), which implies that the high anti-corrosion ability of graphene and larger nuclei size contribute efficaciously to improved reversible Li deposition. However, apparent fading in CE is still found in Gra-0/1-Cu due to the lack of stable SEI film-forming polymer. In comparison, the Gra-5/1-Cu cell maintains the most stable CE of ~96% for more than 250 cycles at 1 mA cm^{-2} and ~95% for around 100 cycles at 2 mA cm^{-2} with 1 mAh cm^{-2}. A larger deposition capacity (3 mAh cm^{-2}) was employed to test their practical application (Fig. 5b). Gra-5/1-Cu still exhibits superior cycling performance at 1 mA cm^{-2} with the highest CE (~98%). In addition, at the low current density (0.5 mA cm^{-2}), the Gra-5/1-Cu cell shows a more stable CE and delivers a longer lifespan for more than 350 cycles compared with Cu at 0.5 mAh cm^{-2} (Fig. S20b). The better electrochemical performance of Gra-5/1-Cu was further verified in the case of ether-based electrolytes at different current densities (Fig. S21). Voltage hysteresis and

reversibility were studied using Cu foil and Gra-5/1-Cu in half cells (Fig. S22). Voltage hysteresis of Gra-5/1-Cu only grows from ~25 mV to ~70 mV, with current density increasing from 0.5 mA cm^{-2} to 3 mA cm^{-2}. In contrast, Cu foil shows dramatic hysteresis change by ~200 mV. In addition, Gra-5/1-Cu also performs the most stable overpotential at 1 mA cm^{-2} (<~60 mV within 400 h) and 2 mA cm^{-2} (<~85 mV within 100 h) with 1 mAh cm^{-2} (Fig. S23a-b). Fig. S24a confirms that the poor cycling of Cu foil is due to weak and non-insulating SEI, other than just surface contaminants like CuO. The above results ultimately prove that the Gra-5/1 can form stable SEI and mitigate the side reactions to stabilize Li deposition.

The GBCC using PAN (Gra-5/1-PAN-Cu) instead of PVDF was prepared to explore the function of polymers (Fig. S24b). The Gra-5/1-PAN-Cu has a long cycling lifetime (>140 cycles), but its CE in the first 30 cycles is ~3% lower than that of Gra-5/1, indicating PVDF is a better film-forming additive. A comparison of cycling lifetime of GBCCs with different PVDF contents (Gra-X/1 (X = 0, 1, 5, and 10)) is shown in Fig. S25a-c. Augmented R_{ct} elucidates that the interface polarization is enhanced when the proportion of PVDF increases (Fig. S25b), aligning with the resistance results (Fig. S8). Fig. S25c demonstrates that an increase in PVDF content can improve cycling lifespan and CE value (within 0-5), but excessive PVDF (e.g., Gra-10/1-Cu) can hinder Li^+ reduction and adversely affect cell performance due to high resistance, resulting in poor cycling stability and low CE. Gra-5/1-Cu also maintains the highest CE value, indicating that the mass ratio of PVDF/graphene=5/1 is probably the best proportion to achieve the dendrite-free and high reversible Li deposit owing to the favourable SEI

and appropriate interface impedance.

To evaluate the performance of Gra-5/1-Cu in full cells, long-term cycling and rate performance of coin full cells assembled with Cu foil or Gra-0/1-Cu or Gra-5/1-Cu and LFP (~2 mAh cm^{-2}) (Fig. S26) or NCM 811 (~4 mAh cm^{-2}) positive electrode (Fig. 5c) were tested. Fig. S26 indicates that Cu-based LFP cell exhibits significant degradation with less than 15% capacity retention after 20 cycles. Gra-0/1-Cu shows a minor enhancement in cycling stability with 45% capacity retention, accompanied by reduced capacity fade rate. However, Gra-5/1-Cu remarkably improves the cycling stability of LMFRBs with ~65% capacity retention, showcasing its effectiveness in stabilizing Li deposition/dissolution. Similarly, the Cu and Gra-0/1-Cu-based NCM811 cells show significantly fast capacity fade to ~45% and ~57% capacity retention, respectively (Fig. 5c). By striking contrast, Gra-5/1-Cu maintains the highest capacity retention of ~71%. Fig. S27 shows that Gra-5/1-Cu exhibits superior rate capability compared to Cu. At 2C, the cell using Gra-5/1-Cu delivers a specific capacity of ~76.9 mAh g^{-1}, significantly higher than that of Cu foil (~46.9 mAh g^{-1}). To further investigate the advantage of Gra-5/1 as a CBCC in Li deposition/dissolution, coin cells were assembled using graphite paper, graphene paper, and expanded graphite paper as pristine 2D CBCCs (Fig. S28a-c). Fig. S28d illustrates that the Gra-5/1-based cell delivers the longest cycling lifespan (>180 cycles) and the highest CE with 1 mAh cm^{-2} at 2 mA cm^{-2}. Meanwhile, Fig. S28e shows that Gra-5/1 exhibits the highest capacity retention after 50 cycles. These results confirm that Gra-5/1 can achieve the *in-situ* construction of favourable SEI and facilitate uniform Li deposition/dissolution with the help of

PVDF.

To further verify the practical applicability of the Gra-5/1 as the CBCC, we assembled pouch cells by using an NCM811 positive electrode (~4 mAh cm^{-2}) with a designed capacity of ~0.16 Ah and normal ester-based electrolyte with a mass of ~0.96 g (Fig. 5d-f). The Cu||NCM 811 cell shows the lowest capacity retention and fastest CE decay within the first 40 cycles at 0.2 C, while both Gra-5/1-Cu and Gra-5/1||NCM 811 cells have much higher capacity retention and similar capacity decay rate, confirming that the electrochemical behaviour of Gra-5/1 is not affected by Cu substrate. Fig. 5e compares the irreversible capacity of every cycle over Cu foil and GBEs after the activation procedure. Irreversible capacity over Cu undergoes dramatic growth from 3^{rd} to 7^{th} and 14^{th} to 16^{th} by 6 and 4 mAh respectively, illustrating violent "dead Li" formation. Irreversible capacity over Gra-0/1-Cu significantly rises to 12 mAh at the 3^{rd} cycle followed by a gradual reduction of irreversible capacity, showing SEI formation is superimposed with "dead Li" generation to lead to the irreversible capacity growth. In solid contrast, irreversible capacity over Gra-5/1-Cu evenly decreases from 6 mAh to 2 mAh during cycling, exhibiting SEI formation is more probably the dominant contribution to the irreversible loss of Li inventory. The Gra-5/1-PAN-Cu||NCM 811(Fig. S24c) and graphite paper||NCM 811 (Fig. S29-S30) pouch cells using a special tab welding technique with Cu stickers and silver paste, as illustrated in the preparation procedure in Fig. S29 were assembled. The capacity retention of these cells was found to be inferior to that of Gra-5/1-based cells, indicating the crucial role of PVDF as a film-forming additive in CBCCs.

Fig. 5f and Fig. S31 compare the internal resistances of pouch cells, which are *in-situ* monitored during cycling. All the pouch cells display a similar trend of an increment of 0.4 Ω in discharge internal resistance (Fig. S31) during the initial 40 cycles. However, Cu||NCM 811 cell shows a significant increase to ~20 Ω, while the others only gradually rise to ~1.1 Ω after 50 cycles. The increased accumulation of "dead Li" on Cu foil plays a vital role in causing a surge in internal resistance. Moreover, the internal resistance of Cu||NCM 811 cell decreases after ~20 cycles, followed by a quick rise after ~40 cycles, which is attributed to the bimodal increase in irreversible capacity on Cu foil (Fig. 5e). Furthermore, Fig. 5f indicates that the PVDF-induced resistance can be forcefully alleviated after the activation procedure possibly owing to the formation of crystal seed, demonstrating the internal resistance of pouch cells cannot be highly affected by the introduction of PVDF. The connection between Cu and Gra-5/1 is stable enough even at high current densities, allowing the pouch cell to normally operate at 1C with low resistance (Fig. S32 a-b).

To investigate the mechanism behind the loss of Li inventory in Cu-based and Gra-5/1-based batteries, cell failure analysis was conducted. Further details can be found in the supporting information (Fig. S33-37). The result shows that the loss of Li inventory in Cu-based cells is primarily caused by the formation of "dead Li", while the loss of Li inventory in Gra-5/1-based cells is mainly due to the generation of by-products (e.g., SEI). More persuasively, fewer "dead Li" can be verified in the Gra-5/1-based LMFRB after 100 cycles compared with Cu-based LMFRBs (Fig. S37). How to decrease the by-products/side reaction between Li and electrolyte on Gra-5/1, especially under lean

electrolyte conditions is the remaining problem to be tackled. Therefore, to further improve the electrochemical performance of Gra-5/1 in LMFRBs, a modified electrolyte with local high concentration designstrategey (electrolyte to capacity ratio (E/C) of ~12 μl mAh^{-1}) was employed in pouch cells using an NCM811 positive electrode (~4 mAh cm^{-2}) with a designed capacity of ~0.38 Ah. A higher salt concentration can enhance the transference number of Li^+ ions, decreasing the local spatial charge variation and alleviating dendrite formation.[41] What's more, local high-concentration electrolytes (fluorine-containing additives) can reduce contact between Li and solvent (DMC), reducing the side product formation.[42, 43] Also, LiDFOB and FSI^- contribute to forming excellent SEI containing Li-F and robust CEI. Consequently, Fig. 5g and Fig. S38 show that the pouch cell as shown in Fig. 5h with Gra-5/1 delivers improved capacity retention (79%) and energy retention (81%) after 50 cycles, respectively. Fig. S39 illustrates that Gra-5/1 still performs 80% capacity retention after 40 cycles even at the lean electrolyte condition (~6 μl mAh^{-1}). The 2.6 Ah multi-layer LMFRBs with high energy density (386 Wh kg^{-1} and 927.5 Wh L^{-1}) were assembled by paring LR-NCM 114 positive electrodes (6 mAh cm^{-2}) with a size of 62 mm × 72 mm with Gra-5/1 (64 mm × 74 mm) (Fig. S40 and Table S2). The pouch cell achieves the discharge energy of 9.3 Wh, demonstrating that Gra-5/1 possesses excellent potential in the practical application of LMFRBs.

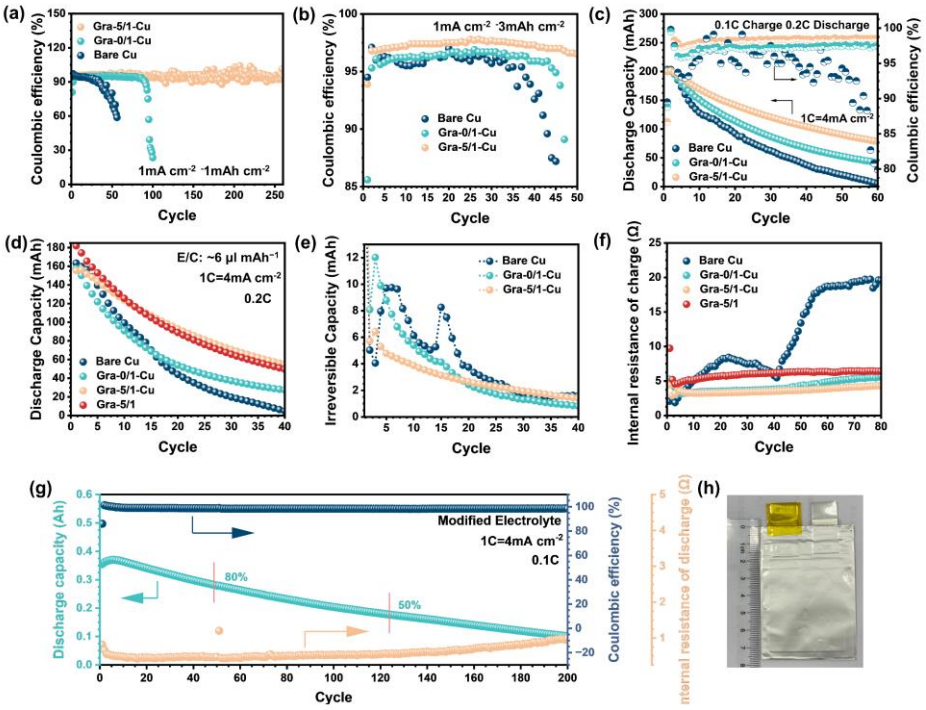

Fig. 5. Electrochemical performances of Cu-based and graphene-based cells. Comparison of CE of Li plating/stripping with the capacity of (a) 1 mAh·cm^{-2} and (b) 3 mAh·cm^{-2} at 1 mA cm^{-2} over bare Cu, Gra-0/1-Cu, and Gra-5/1-Cu. (c) Cycling performance of coin full cells assembled with bare Cu, Gra-0/1-Cu, and Gra-5/1-Cu and NCM 811 positive electrode (~ 4 mAh cm^{-2}). (d) Cycling performance, (e) irreversible capacity and (f) *in-situ* discharge internal resistance profiles of pouch cells assembled with bare Cu, Gra-0/1-Cu, Gra-5/1-Cu, and Gra-5/1 and NCM 811 positive electrode (~ 4 mAh cm^{-2}). (g) The discharge capacity profiles of a pouch cell assembled with Gra-5/1 and NCM 811 positive electrode (~ 4 mAh cm^{-2}) using the modified electrolyte. (h) Optical photo of the pouch cell.

4 Conclusion

In brief, a free-standing GBCC with a Cu tab is fabricated to replace Cu foil in practical pouch cells. Tightly stacked graphene sheets can decrease the lithiation and extra Li consumption (SEI). PVDF, acting as a superior binding agent, strengthens the

mechanical properties of CBCCs effectively, thereby mitigating the issue of expansion and lithiation in practical conditions. Consequently, the composite CBCCs meet the fundamental criteria of current collectors, including acceptable conductivity, good mechanical strength, and feasible tab welding. In addition, PVDF is an exceptional film-forming polymer that plays a key role in the formation of highly insulating and Li-F-rich SEI. By mitigating the escape of electrons and promoting uniform Li^+ flux, this stable interface helps to facilitate dendrite-free Li deposition, ultimately leading to improved reversible Li capacity in pouch cells. The failure analysis of batteries has revealed that bulk generation of "dead Li" is responsible for the consumption of the Li source and the resultant increase in internal resistance in Cu-based LMFRBs. In contrast, by-product generation is the primary cause of gradual capacity decay in Gra-5/1-based LMFRBs. Based on the suggestion from failure analysis, the Gra-5/1-based pouch cell using modified electrolyte achieves capacity retention of 80% after ~50 cycles with a high plating capacity of 4 mAh cm^{-2}. It is believed that the low density and high efficiency of this composite CBCC can significantly contribute to the achievement of high specific energy in LMFRBs.

Supporting Information

Supporting Information is available from the Wiley Online Library or the author.

Acknowledgments

This work was supported by the National Natural Science Foundation of China

(Grant No. 51872305, 52001320). Qiang Guo appreciates the Doctoral Training Partnership Programme supported by the University of Nottingham Ningbo, China, and Ningbo Institute of Materials Technology & Engineering, Chinese Academy of Sciences. Qiang Guo also thanks the Chinese Scholarship Fund provided by the China scholarship council to pursue studies in the UK (File No. 202108330377).

Conflict of Interest

The authors declare no conflict of interest.

References

1. Guo, Q.; Deng, W.; Xia, S.; Zhang, Z.; Zhao, F.; Hu, B.; Zhang, S.; Zhou, X.; Chen, G. Z.; Liu, Z., *Nano Research* **2021,** *14* (10), 3585-3597.

2. Xie, Z.; Wu, Z.; An, X.; Yue, X.; Wang, J.; Abudula, A.; Guan, G., *Energy Storage Materials* **2020,** *32*, 386-401.

3. Lin, D.; Liu, Y.; Cui, Y., *Nature Nanotechnology* **2017,** *12* (3), 194-206.

4. Chen, W.; Salvatierra, R. V.; Ren, M.; Chen, J.; Stanford, M. G.; Tour, J. M., *Advanced Materials* **2020,** *32* (33), 2002850.

5. Zhang, S. S.; Fan, X.; Wang, C., *Electrochimica Acta* **2017,** *258*, 1201-1207.

6. Pande, V.; Viswanathan, V., *ACS Energy Letters* **2019,** *4* (12), 2952-2959.

7. Kwon, H.; Lee, J.-H.; Roh, Y.; Baek, J.; Shin, D. J.; Yoon, J. K.; Ha, H. J.; Kim, J. Y.; Kim, H.-T., *Nature Communications* **2021,** *12* (1), 5537.

8. Lu, Z.; Liang, Q.; Wang, B.; Tao, Y.; Zhao, Y.; Lv, W.; Liu, D.; Zhang, C.; Weng, Z.; Liang, J.; Li, H.; Yang, Q.-H., *Advanced Energy Materials* **2019,** *9* (7), 1803186.

9. Xie, J.; Ye, J.; Pan, F.; Sun, X.; Ni, K.; Yuan, H.; Wang, X.; Shu, N.; Chen, C.; Zhu, Y., *Adv Mater* **2019,** *31* (7), 1805654.

10. Assegie, A. A.; Cheng, J.-H.; Kuo, L.-M.; Su, W.-N.; Hwang, B.-J.,

Nanoscale **2018,** *10* (13), 6125-6138.

11. Wondimkun, Z. T.; Beyene, T. T.; Weret, M. A.; Sahalie, N. A.; Huang, C.-J.; Thirumalraj, B.; Jote, B. A.; Wang, D.; Su, W.-N.; Wang, C.-H.; Brunklaus, G.; Winter, M.; Hwang, B.-J., *Journal of Power Sources* **2020,** *450*, 227589.

12. Qian, J.; Adams, B. D.; Zheng, J.; Xu, W.; Henderson, W. A.; Wang, J.; Bowden, M. E.; Xu, S.; Hu, J.; Zhang, J.-G., *Advanced Functional Materials* **2016,** *26* (39), 7094-7102.

13. Weber, R.; Genovese, M.; Louli, A. J.; Hames, S.; Martin, C.; Hill, I. G.; Dahn, J. R., *Nature Energy* **2019,** *4* (8), 683-689.

14. Wang, H.; Yu, Z.; Kong, X.; Huang, W.; Zhang, Z.; Mackanic, D. G.; Huang, X.; Qin, J.; Bao, Z.; Cui, Y., *Advanced Materials* **2021,** *33* (25), 2008619.

15. Genovese, M.; Louli, A. J.; Weber, R.; Hames, S.; Dahn, J. R., *Journal of The Electrochemical Society* **2018,** *165* (14), A3321-A3325.

16. Genovese, M.; Louli, A. J.; Weber, R.; Martin, C.; Taskovic, T.; Dahn, J. R., *Journal of The Electrochemical Society* **2019,** *166* (14), A3342-A3347.

17. Lin, L.; Suo, L.; Hu, Y. s.; Li, H.; Huang, X.; Chen, L., *Advanced Energy Materials* **2021,** *11* (9), 2003709.

18. Assegie, A. A.; Chung, C. C.; Tsai, M. C.; Su, W. N.; Chen, C. W.; Hwang, B. J., *Nanoscale* **2019,** *11* (6), 2710-2720.

19. Lang, J.; Song, J.; Qi, L.; Luo, Y.; Luo, X.; Wu, H., *ACS Applied Materials & Interfaces* **2017,** *9* (12), 10360-10365.

20. Kolesnikov, A.; Kolek, M.; Dohmann, J. F.; Horsthemke, F.; Börner, M.; Bieker, P.; Winter, M.; Stan, M. C., *Advanced Energy Materials* **2020,** *10* (15), 2000017.

21. Lin, D.; Liu, Y.; Liang, Z.; Lee, H.-W.; Sun, J.; Wang, H.; Yan, K.; Xie, J.; Cui, Y., *Nature Nanotechnology* **2016,** *11* (7), 626-632.

22. Deng, W.; Zhu, W.; Zhou, X.; Liu, Z., *Energy Storage Materials* **2018,** *15*, 266-273.

23. Wang, Z. Y.; Lu, Z. X.; Guo, W.; Luo, Q.; Yin, Y. H.; Liu, X. B.; Li, Y. S.; Xia, B. Y.; Wu, Z. P., *Advanced Materials* **2021,** *33* (4), 2006702.

24. Menkin, S.; O'Keefe, C. A.; Gunnarsdóttir, A. B.; Dey, S.; Pesci, F. M.; Shen, Z.; Aguadero, A.; Grey, C. P., *Journal of Physical Chemistry C* **2021,** *125* (30), 16719-16732.

25. Khan, J.; Momin, S. A.; Mariatti, M., *Carbon* **2020,** *168*, 65-112.

26. Meng, Q.; Deng, B.; Zhang, H.; Wang, B.; Zhang, W.; Wen, Y.; Ming, H.; Zhu, X.; Guan, Y.; Xiang, Y.; Li, M.; Cao, G.; Yang, Y.; Peng, H.; Zhang, H.; Huang, Y., *Energy Storage Materials* **2019,** *16*, 419-425.

27. Sonia, F. J.; Ananthoju, B.; Jangid, M. K.; Kali, R.; Aslam, M.; Mukhopadhyay, A., *Carbon* **2015,** *88*, 206-214.

28. Yoo, D. J.; Elabd, A.; Choi, S.; Cho, Y.; Kim, J.; Lee, S. J.; Choi, S. H.; Kwon, T. w.; Char, K.; Kim, K. J.; Coskun, A.; Choi, J. W., *Advanced Materials* **2019,** *31* (29), 1901645.

29. Chu, H.-C.; Tuan, H.-Y., *Journal of Power Sources* **2017,** *346*, 40-48.

30. Papageorgiou, D. G.; Kinloch, I. A.; Young, R. J., *Progress in Materials Science* **2017,** *90*, 75-127.

31. Guo, Q.; Yu, Y.; Xia, S.; Shen, C.; Hu, D.; Deng, W.; Dong, D.; Zhou, X.; Chen, G. Z.; Liu, Z., *ACS Applied Materials & Interfaces* **2022,** *14* (40), 46043-46055.

32. Guo, Y.; Niu, P.; Liu, Y.; Ouyang, Y.; Li, D.; Zhai, T.; Li, H.; Cui, Y., *Advanced Materials* **2019,** *31* (27), 1900342.

33. Lin, Y.-X.; Liu, Z.; Leung, K.; Chen, L.-Q.; Lu, P.; Qi, Y., *Journal of Power Sources* **2016,** *309*, 221-230.

34. Wang, L.; Luo, G., *Nano Letters* **2021,** *21* (17), 7284-7290.

35. Cook, B.; Russakoff, A.; Varga, K., *Applied Physics Letters* **2015,** *106* (21), 211601.

36. Liao, X.; Liu, Q.; Liu, X.; Zhu, S.; Zhao, K.; Zhao, Y., *Phys Chem Chem Phys* **2022,** *24* (8), 4751-4758.

37. Sun, S.; Myung, S.; Kim, G.; Lee, D.; Son, H.; Jang, M.; Park, E.; Son, B.; Jung, Y.-G.; Paik, U.; Song, T., *Journal of Materials Chemistry A* **2020,** *8* (33), 17229-17237.

38. Lang, J.; Long, Y.; Qu, J.; Luo, X.; Wei, H.; Huang, K.; Zhang, H.; Qi, L.; Zhang, Q.; Li, Z.; Wu, H., *Energy Storage Materials* **2019,** *16*, 85-90.

39. Hou, Z.; Gao, Y.; Zhou, R.; Zhang, B., *Advanced Functional Materials* **2021,** *32* (7).

40. Mashreghi, A.; Zare, H., *Current Applied Physics* **2016,** *16* (5), 599-604.

41. Li, M.; Lu, J.; Ji, X.; Li, Y.; Shao, Y.; Chen, Z.; Zhong, C.; Amine, K., *Nature Reviews Materials* **2020,** *5* (4), 276-294.

42. Ren, X.; Chen, S.; Lee, H.; Mei, D.; Engelhard, M. H.; Burton, S. D.; Zhao, W.; Zheng, J.; Li, Q.; Ding, M. S.; Schroeder, M.; Alvarado, J.; Xu, K.; Meng, Y. S.; Liu, J.; Zhang, J.-G.; Xu, W., *Chem* **2018,** *4* (8), 1877-1892.

43. Ren, X.; Zou, L.; Cao, X.; Engelhard, M. H.; Liu, W.; Burton, S. D.; Lee, H.; Niu, C.; Matthews, B. E.; Zhu, Z.; Wang, C.; Arey, B. W.; Xiao, J.; Liu, J.; Zhang, J.-G.; Xu, W., *Joule* **2019,** *3* (7), 1662-1676.